Journal of Nuclear Medicine, published on February 11, 2016 as doi:10.2967/jnumed.115.163493

microPET Imaging of Tau Pathology with ^{18}F-THK5117 in two Transgenic Mouse Models

Brendel Matthias[1*], Jaworska Anna[2*], Probst Federico[1], Overhoff Felix[1], Korzhova Viktoria[2], Lindner Simon[1], Carlsen Janette[1], Bartenstein Peter[1,3], Harada Ryuichi[4], Kudo Yukitsuka[4], Haass Christian[2,3,5], Van Leuven Fred[6], Okamura Nobuyuki[4], Herms Jochen[2,3], Rominger Axel[1,3]

[1]Dept. of Nuclear Medicine, Ludwig-Maximilians-University of Munich, Munich, Germany
[2]German Center for Neurodegenerative Diseases (DZNE), Munich, Germany
[3]Munich Cluster for Systems Neurology (SyNergy), Munich, Germany
[4]Tohoku University, Sendai, Japan
[5]Biomedical Center (BMC), Ludwig-Maximilians-University of Munich, Munich, Germany
[6]Experimental Genetics Group LEGTEGG,KU-Leuven, Belgium

Running title: ^{18}F-THK5117 µPET in transgenic mice

* Both authors contributed equally

Financial Support: The study was financially supported by the SyNergy Cluster and the Friedrich-Baur-Stiftung.

Word count: 4999

First author:

Dr. Matthias Brendel, Marchioninistr. 15, 81377 Munich, Germany; Phone: +49(0)89440074646; Fax: +49(0)89440077646; Email: matthias.brendel@med.uni-muenchen.de; resident

Corresponding author:

Prof. Dr. Axel Rominger, Marchioninistr.15; 81377 Munich, Germany; Phone: +49(0)89440074650; Fax: +49(0)89440077646; E-Mail: axel.rominger@med.uni-muenchen.de

ABSTRACT

Abnormal accumulation of tau aggregates in brain is one of the hallmarks of Alzheimer's disease neuropathology. We visualized tau deposition *in vivo* with the previously developed 2-arylquinoline derivative ^{18}F-THK5117 using small animal positron-emission-tomography (μPET) in conjunction with autoradiography and immunohistochemistry gold standard assessment in two transgenic mouse models expressing hyperphosphorylated tau. μPET recordings were obtained in groups of P301S (N=11) and biGT mice (N=16) of different ages, with age-matched wild-type (WT) serving as controls. After i.v. administration of 16±2 MBq ^{18}F-THK5117, a dynamic 90 min emission recording was initiated for P301S mice and during 20-50 min p.i. for biGT mice, followed by a 15 min transmission scan (Siemens Inveon DPET). After co-registration to the MRI atlas and scaling to the cerebellum, we performed volume-of-interest based analysis (standard-uptake-value-ratio, SUVR) and statistical parametric mapping (SPM). μPET results were compared with autoradiography *ex vivo* and *in vitro*, and further validated with AT8 staining for neurofibrillary tangles. SUVRs calculated from static recordings during the interval of 20–50 min after tracer injection correlated highly with estimates of BP_{ND} based on the entire dynamic emission recordings (R=0.85). SUVR increases were detected in brainstem of aged P301S mice (+11%; p<0.001), and in entorhinal/amygdaloidal areas (+15%; p<0.001) of biGT mice when compared to WT, whereas aged WT mice did not show increased tracer uptake. Immunohistochemical tau loads correlated with μPET-SUVR for both P301S (R=0.8; p<0.001) and biGT (R=0.7; p<0.001) mice,

and distribution patterns of AT8 positive neurons matched voxel-wise SPM analysis. Saturable binding of the tracer was verified by autoradiographic blocking studies. In the first dedicated μPET study in two different transgenic tauopathy mouse models using the novel tau tracer ^{18}F-THK5117, the temporal and spatial progression could be visualized in good correlation with gold standard assessments of tau accumulation. Serial μPET method could afford the means for preclinical testing of novel therapeutic approaches by accommodating inter-animal variability at baseline, while detection thresholds in young animals have to be considered.

Keywords: Alzheimer's disease; tauopathy; small animal PET; transgenic mice; ^{18}F-THK5117

INTRODUCTION

Alzheimer's disease (AD) is the most frequent cause of dementia, with an exponentially increasing incidence as a function of age among the elderly. This epidemic is imposing an increasingly onerous burden on health care in societies with aging populations (*1*). There is an urgent need to find new biomarkers predictive of clinical course, and also serving as outcome measures in clinical trials of innovative disease-modifying agents (*2*). The main neuropathological features of AD, which include the accumulation of extracellular β-amyloid plaques and intracellular neurofibrillary tangles (*3*), are emulated in transgenic animal models (*4-6*). Micro positron-emission-tomography (μPET) has emerged as a useful tool for translational research involving longitudinal *in vivo* imaging of β-amyloid and tau pathology in rodent models (*7, 8*).

While β-amyloid μPET in transgenic mice has been successfully established for preclinical *in vivo* imaging (*9-11*), there have been few reports on tau-μPET data in wild-type (WT) and transgenic mice (*12, 13*). Successful molecular imaging with ^{18}F-fluorinated radiotracers of neurofibrillary tangle accumulation is a recent development (*14*); the 2-arylquinoline derivative ^{18}F-THK5117 has shown high affinity for neurofibrillary tangles *in vitro* and in brain sections from AD patients (*13*). However, the suitability of this agent for monitoring the accumulation of neurofibrillary tangles by μPET in mice with tau pathology remains to be established.

The aim of this μPET study was therefore to investigate the sensitivity of μPET with the novel tracer ^{18}F-THK5117 in two transgenic mouse models with

tau overexpression, and to compare several approaches for μPET quantitation, validated relative to immunohistochemistry, and additionally by autoradiography in vitro.

MATERIALS AND METHODS

Radiochemistry

Radiosynthesis of ^{18}F-THK5117 was performed as previously described (*15*) with slight modifications detailed in Supplementary Methods, yielding a radiochemical purity >98%, and specific activity of 202±56 GBq/μmol at end of synthesis.

Animals

All experiments were carried out in compliance with the National Guidelines for Animal Protection (Germany) and approval of the animal care committee (Regierung Oberbayern), with supervision by a veterinarian. Two transgenic (TG) mouse models were investigated in this study: Tau-P301S mice (P301S) and bigenic GSK-3β x Tau-P301L (biGT) mice, together with age-matched WT controls. Details on the animal models are provided in Supplementary Methods.

Tau μPET

Study Overview. A detailed overview of the different groups of mice and investigations performed is presented in Table 1. Test-retest μPET scans were

acquired in a subset of seven P301S and C57Bl/6 animals within one week, using identical scanning parameters. To investigate the optimal time window for μPET quantitation, complete 90 min dynamic recordings were acquired in P301S and corresponding WT mice; findings from these pilot scans defined the optimal acquisition window to be employed in the larger biGT cohort.

Data Acquisition and Analyses. For data acquisition and reconstruction see Supplementary Methods for details. In brief, summed dynamic (0-90 min p.i. for P301S) and static frames (20-50 min p.i. for biGT) were co-registered to an MRI mouse atlas (*16*) by a manual rigid-body transformation (TX_{rigid}) using the PMOD fusion tool (V3.5, PMOD Technologies Ltd.). The reader was blind to the type of mouse. A second experienced reader ensured accurate alignment. Volumes-of interest were defined on the MRI mouse atlas (Fig. 1). In P301S animals receiving the full dynamic μPET scan, parametric maps of binding potential (BP_{ND}) were calculated using a linear graphic method (*17*), with the cerebellar VOI serving as pathology-free reference tissue. Time-activity-curves of brainstem, cranium, Harderian glands, and whole brain were extracted. Reference and target VOIs were employed for calculation of ^{18}F-THK5117 brainstem-to-cerebellum ($SUVR_{BST/CBL}$ in P301S) and entorhinal/amygdaloidal-to-cerebellum standardized uptake value ratios ($SUVR_{ENT/CBL}$ in biGT) of the 20-50 min frame.

Reader Independent Coregistration. For final VOI- and SPM-based µPET analyses, a reader-independent coregistration was established after validation of the optimal 20-50 min window. Further details are provided in Supplementary Methods.

SPM. For whole-brain voxel-wise comparisons between groups of TG versus pooled WT mice, SPM was performed using SPM5 routines (Wellcome Department of Cognitive Neurology, London, UK) implemented in MATLAB (version 7.1) (*10*). Individual SUV maps from TG mice were also compared with pooled WT mice to calculate for each mouse a voxel-wise Z-score map expressing the divergence in standard deviations (SDs) from the WT group. Furthermore, we performed linear regression with tau load (%) as a vector in the entire groups of (young and old) P301S and biGT mice.

Immunohistochemistry

After completion of the final µPET scans, phosphorylated tau was detected in postfixed brains with the monoclonal AT8 antibody (Thermo Scientific), which recognizes phospho-PHF-tau, phosphorylated at Ser202 and Thr205. A more detailed description of immunohistochemistry is provided in Supplementary Methods. Tau load (%) was calculated as the summed area of all tau positive cells relative to the area of regions of interest. These analyses were performed by an operator blind to the µPET results.

Ex Vivo and *In Vitro* Autoradiography

Ex vivo autoradiography was performed in a subset of P301S and C57Bl/6 animals killed while deeply anesthetized at 50 min after injection of 15.2±3.4 MBq ^{18}F-THK5117, administered in 150µl saline to a tail vein. *In vitro* autoradiography was performed in these and further mice; for an overview of methods see Table 1. A detailed description of the procedure is provided in Supplementary Methods.

Statistics

Group comparisons of VOI-based µPET results between TG cohorts and WT mice were assessed by one-way ANOVA and the Tukey post-hoc test for multiple comparisons using IBM SPSS Statistics (version 22.0; SPSS, Chicago, IL). For correlation analyses, Pearson's coefficients of correlation (R) were calculated. A threshold of $p<0.05$ was considered to be significant for rejection of the null hypothesis. For the voxel-wise group comparison of TG versus WT mice, 2-sample *t*-tests were performed, with a significance threshold of $p<0.001$, uncorrected for multiple comparisons.

RESULTS

Dynamic VOI-based Analyses and Methodology

VOI-based analyses of the dynamic µPET data from P301S and C57Bl/6 mice were performed to investigate ^{18}F-THK5117 kinetics in the brain in relation to the influence of spillover from extracerebral structures, and to define an optimal time window for static µPET recordings. Mean (±SD) brainstem-to-

cerebellum ratios in P301S mice aged 5.5 and 8-11 months and for pooled WT mice aged 6-12 months are shown in Fig. 2A. Extracerebral activities (cranium, Harderian glands) in relation to whole brain activity are shown in Fig. 2B. The time-activity curves suggest the attainment of equilibrium binding in brain by about 15 min p.i.. Cranial uptake exceeded brain activity at times after 25 min, and progressive uptake in Harderian glands gives rise to potential cerebral spill-in after 50 min. These findings together suggested the use of an early static time frame in order to avoid distortion of brain time-activity-curves. Additionally attention was required for assessing ^{18}F-THK5117 uptake in the frontal brain as this region was potentially vulnerable to spill-in from the Harderian glands, even at early time points.

There was a high correlation of BP_{ND} in all VOIs calculated for the entire 90 minute recordings, with the SUVR (R=0.85, p<0.001) for the time frame 20-50 min post-injection (Fig. 2C). Test-retest analyses showed 20-50 min $SUVR_{BST/CBL}$ values in the entire study group to be robust for the brainstem target region (R=0.95, p<0.001; Fig. 2D). The mean variability in test-retest in that VOI was 1.2%, with maximum variability of 2.5%.

VOI-based μPET analyses

VOI-based analyses revealed significant SUVR differences in the brainstem of aged P301S animals compared to pooled WT mice (+11%; p<0.001) (Fig. 3A; Table 1). In the younger P301S mice examined at the age of 5.5 months, the brainstem signal was in the range of WT mice (1.18±0.04 vs.

1.16±0.05). There was a significantly higher ^{18}F-THK5117 uptake in the entorhinal cortex/amygdala VOI from biGT mice at 12 (+14.9%; p<0.001) and 21 months of age (+15.2%; p<0.001) compared to pooled WT mice (Fig. 3B; Table 1).

Voxel-wise Analyses

Voxel-wise group contrasts between TG and WT animals are shown in Fig. 4. From this exploratory approach we could discern significant differences in ^{18}F-THK5117 uptake between P301S and pooled WT mice in a brainstem cluster (3,105 voxels; p<0.01). The largest uptake differences in biGT versus pooled WT SUVR were found in a cluster comprising the entorhinal and piriform cortices as well as in the amygdalo-hippocampal formation and the lateral hypothalamus at 12 (109,366 voxels; p<0.001) and 21 (138,786 voxels; p<0.001) months of age. Smaller clusters for both biGT groups were also observed in the parietal and frontal neocortex (12 mo: 6,204 voxels; p<0.001 / 21 mo: 6,605 voxels; p<0.001), whereas an additional cluster spreading along the piriform and orbitofrontal cortices and into the basal forebrain (17,630 voxels; p<0.001) was distinctly apparent in aged biGT mice.

Immunohistochemical Validation

P301S mice revealed AT8-positive tau deposition predominantly in the brainstem, and penetrating into the cerebellar peduncles, lesser amounts in the forebrain, and complete absence in the cerebellar hemispheres. In the two mice

examined at the age of 5.5 months, the brainstem tau loads were 10% and 11%, while in 8-11 month old P301S mice, the mean brainstem tau load was 39±20% (N=7; range: 15–65%). μPET results correlated highly with the immunohistochemical quantitation of tau deposits in brainstem ($R=0.8$; $p<0.001$; Fig. 5A). A cluster of significant correlation was found in the central part of the brainstem (4,078 voxels; $p<0.05$; Fig. 5A), while the patterns of Z-score maps deriving from single mouse SPM were consistently congruent with the pattern of AT8 staining (Fig. 5A).

biGT mice showed a distinct regional distribution of AT8 positive tau deposits, with highest amounts in the entorhinal/piriform cortex and the adjacent amygdala, followed by the hippocampal formation, and with lesser amounts in the basal forebrain . One of eight mice aged 12 months was tau negative; the mean entorhinal/amygdala tau load of 11.4±7.4% (range 0.0–19.4%). All biGT mice aged 21 months had tau deposits, with a group mean tau load in the inferior temporal region of 14.3±5.8% (range 8.5–23.8%; n.s. versus TG 12 months). μPET results correlated highly with the immunohistochemical findings in the entorhinal/amygdala VOI ($R=0.7$; $p<0.001$; Fig. 5B). The two measures correlated significantly in bilateral clusters centered on the amygdala (49,788 voxels; $p<0.01$; Fig. 5B), while the Z-score maps from single mouse SPM were also congruent with the AT8 staining pattern (Fig. 5B).

Autoradiography and Blocking Experiments

Representative autoradiographic findings *ex vivo* and *in vitro* in P301S and C57Bl/6 animals are illustrated along with corresponding µPET binding ratio images in Figs. 6A and 6B. In biGT mice complete blocking of saturable radioligand binding was achieved by addition of cold radioligand (Fig. 6C).

DISCUSSION

We present the first µPET study with a ^{18}F-labelled radiotracer for hyperphosphorylated tau in large groups of two distinct transgenic mouse models and in WT littermates. µPET imaging with ^{18}F-THK5117 affords sensitive discrimination of tau pathology between both transgenic strains and WT animals, despite the several challenges presented by limited spatial resolution relative to the scale of target structures, low specific signal, and the inherent inter-animal variability of tau deposition. Indeed, considerable stability of our µPET procedure for *in vivo* quantitation of hyperphosphorylated tau burden was proven in test-retest studies, and µPET gave results concurring closely with immunohistochemical findings and autoradiography. The detection of tauopathy, which is generally hampered by high unspecific background binding of the tracer, was enhanced by voxel-wise SPM approaches.

Reference Region and Scan Window

The configuration of a suitable reference tissue region for the analysis of µPET brain imaging of the rodent brain is critical. The reference region must be

devoid of the targeted binding site or pathology, and should provide robust reference values for semiquantitative analyses of the tau pathology (*14*). Our present immunohistochemical analysis showed some tau deposition in the cerebellar peduncles of aged P301S mice. Therefore, we were obliged to edit the cerebellum template so as to avoid this source of specific binding signal, which might otherwise have biased the estimation of BP_{ND} in VOIs (*18*).

Dynamic μPET shows that ^{18}F-THK5117 rapidly attains a plateau concentration in living mouse brain, while radioactivity continues to accumulate in certain extracerebral regions during prolonged μPET scans. Radioactivity in the cranium, which reflects defluorination of the tracer, increases linearly with time, exceeding the global cerebral mean uptake at times after 30 min p.i.. However, intense bone uptake was present only in four animals, and was most prominent in foci within the frontal bone; as we have noted earlier in mouse μPET with the dopamine receptor tracer ^{18}F-desmethoxyfallypride (*19*), we do not expect substantial brain spill-in arising from bone for ^{18}F-THK5117 scans lasting less than 60 min. However, the linear uptake in the Harderian glands soon becomes substantial, and could well contaminate brain signal during late acquisition frames, especially for the nearby frontal cortex. This possibility was minimized through our use of early acquisition frames. In any case, we find that binding ratios attain a stable equilibrium in only ten minutes. Binding ratios from the 20-50 min static frame correlated very well with BP_{ND} values from full dynamic recordings lasting 90 minutes. Thus, this early time window serves admirably as a convenient surrogate of the more physiologically-defined BP_{ND}. Furthermore,

with brief scans, the duration of anaesthesia is minimized without compromising the sensitivity of the endpoint measure.

Background / Low Binding

Although SUVR values in target regions are significantly higher in P301S and biGT mice than in their controls, the magnitude of the ratios is low, even in regions with demonstrably high tau deposition. Two factors should be considered in this regard; First, the ^{18}F-THK5117 background binding, especially in regions with abundant white matter (i.e. the brainstem) is relatively high, and consequently hampers the detection of specific binding signal, even in those regions with high tau deposition. This limitation of ^{18}F-THK5117 μPET is made clear by comparing unspecific binding in WT mice and the increment in tau-positive animals, which seldom exceeds 20%, despite heavy tau load in target regions. Thus, for example, increments are relatively low in the "high-background" brainstem target region of aged P301S animals (1.17 SUVR background in WT; 11% difference in TG mice with 38% tau load). Quantitation is more favoured in the "low-background" entorhinal cortex/amygdala target region of biGT mice (1.01 SUVR background in WT; 15% difference in TG with 14% tau load). We do note that an earlier investigation with ^{18}F-THK523 in rTG4510 mice (*20*) found 48% higher global brain uptake when compared to WT (*21*). We cannot fully account for this discrepancy, but suppose that different methodological approaches and strain-dependent tracer kinetics may be relevant factors.

A second factor in our relatively low target binding ratios might be related to the imperfect concordance of ^{18}F-THK5117 binding to the prevailing conformation of the tau deposits in fronto-temporal dementia (FTLD) mice (*22*). Although the exact binding site of radiotracers to tau-fibrils remains to be identified, the paired helical filaments (PHF) described in post mortem AD material are more effectively targeted by 2-arylquinolines than is the tauopathy in FTLD (*23*). Present data allow us to predict that the higher signal in μPET relative to the lower tau deposition in biGT mice (in contrast to P301S) may be indicative of a more AD-like phosphorylation induced by GSK3-β, resulting in a fibrillar aggregation more similar to that observed in AD brain (*24*). Nevertheless, the saturable ^{18}F-THK5117 binding in regions with high tau deposition in both mouse models was blocked by cold tracer. We used AT8 immunohistochemistry to confirm staining of tau aggregates (*25*) which showed colocalization with methoxy-X04 stained β-sheet structures (see Supplementary Fig. 2). While aged P301S mice contain mainly FTLD-like half-twisted ribbons, they also express AD-like PHFs (*26*). It remains a challenge to elucidate the affinities of ^{18}F-THK5117 for the tau conformations prevailing in different transgenic mouse models; indeed, this should be a priority to be addressed in future studies.

Voxel-wise Approach

Tau depositions in P301S and biGT mice are not restricted to foci, but rather occur at multiple sites encompassing wide parts of the cerebrum, as is likewise the case for tau distribution in human AD pathology (*27*). Nonetheless,

some differences in distribution are evident in the present TG mouse models. Thus, VOI-based analyses of tau-rich regions in groups of TG mice are feasible, but may miss individual heterogeneities in tau pathology. In this regard, voxel-wise analyses present distinct advantages by interrogating tau levels in each voxel of the mouse brain, without prior assumptions of distribution patters in individuals (Supplementary Fig. 1). Statistically-defined voxel clusters of increased ^{18}F-THK5117 binding in our TG mouse groups matched the immunohistochemical patterns, validating group comparisons by these methods (Fig. 4). However, z-score analyses in single mice proved fit for monitoring tauopathy in brain of individual mice (Fig. 5). Voxel-wise comparisons present similar advantages for monitoring β-amyloid deposition by μPET (*10*).

Suitability for *in vivo* Therapy Monitoring

Despite the massive (60%) tau load in certain affected regions of aged P301S mice, we found an SUVR of only 11% increase by μPET. As noted above, this discrepancy may be related to conformational hindrance of ligand binding in vivo. Moreover P301S mice aged 8-11 months are moribund, and intolerant of narcosis compared to age-matched controls. Thus, P301S mice may not present a favourable model for prospectively monitoring anti-tau treatments by serial ^{18}F-THK5117 μPET studies.

In contrast, biGT mice offer a longer life-span, as their motor function is much less affected by tau pathology, and they manifestly tolerate narcosis and μPET scans even at the very old age of 21 months. We observed regional

variability in the tau deposition in entorhinal/amygdala and hippocampus regions (Supplementary Fig. 1), but only a slight increase in tau binding between 12 and 21 months of age. As such, the biGT model may not be ideally suited for longitudinal intervention studies. However, as in our earlier experience with β-amyloid mice, sensitive detection of treatment effects should be enhanced by undertaking individual baseline μPET recordings, so as to accommodate better the variability of the trajectories of pathology; baseline scanning can also be used to assign individual animals so as to obtain optimally matched subgroups, as proposed in our earlier work (*28*). The P301S and biGT models both showed rather high detection threshold to μPET, corresponding to approximately ≥10% tau load based on gold standard histopathological examination. Although tau load is thus difficult to quantify in young animals, the robust detection by ^{18}F-THK5117 μPET in older mice should afford the necessary sensitivity to support studies of interventional therapy.

Limitations

Issues dealing with the frontal hot spot, translational aspects as well as background of control animals can be found in Supplementary Limitations.

CONCLUSION

Preclinical *in vivo* imaging of tau pathology by mouse μPET is feasible, and gives results strongly correlating with immunohistopathological and autoradiographic gold standard estimates. The logistically convenient 20-50 min

p.i. acquisition after intravenous ^{18}F-THK5117 injection yields robust and reproducible SUVR values, and greatly minimizes the risk of cerebral spill-over from cranium and extracerebral sources. The relatively low ^{18}F-THK5117 target-to-reference ratios in the mouse brain need to be considered, but can be compensated by voxel-wise SPM data analysis, which improves the sensitivity for detecting regional gradients in the tau pathology in single animals. *In vivo* assessment of the characteristic inter-animal heterogeneity in tau accumulation may well enhance the statistical power of future interventional studies with follow-up to individual baseline levels. A matter still to be resolved is the impact of strain-specific configurations of tau deposition on µPET studies with ^{18}F-THK5117.

ACKNOWLEDGMENTS

A part of this paper originated from the doctoral thesis of Federico Probst. We thank Karin Bormann-Giglmaier and Rosel Oos for excellent technical assistance. We thank the LEGTEGG (KULeuven) alumni for their technical and scientific contributions. The authors acknowledge *Inglewood Biomedical Editing* for professional editing of the manuscript.

DISCLOSURE

The study was financially supported by the SyNergy Cluster (Peter Bartenstein, Christian Haass, Jochen Herms and Axel Rominger) and by the Friedrich-Baur-Stiftung (73/15). Anna Jaworska was supported by the Foundation for Polish Science within the International PhD Project ‘Studies of nucleic acids and proteins – from basic to applied research’, co-financed from European Union - Regional Development Fund; MPD/2009-3/2.

REFERENCES

1. Ziegler-Graham K, Brookmeyer R, Johnson E, Arrighi HM. Worldwide variation in the doubling time of Alzheimer's disease incidence rates. *Alzheimers Dement.* 2008;4:316-323.

2. Weiner MW, Veitch DP, Aisen PS, et al. The Alzheimer's Disease Neuroimaging Initiative: A review of papers published since its inception. *Alzheimers Dement.* 2012;8:S1-S68.

3. Duyckaerts C, Delatour B, Potier MC. Classification and basic pathology of Alzheimer disease. *Acta Neuropathol.* 2009;118:5-36.

4. Denk F, Wade-Martins R. Knock-out and transgenic mouse models of tauopathies. *Neurobiol Aging.* 2009;30:1-13.

5. Hall AM, Roberson ED. Mouse models of Alzheimer's disease. *Brain Res Bull.* 2012;88:3-12.

6. Teipel SJ, Buchert R, Thome J, Hampel H, Pahnke J. Development of Alzheimer-disease neuroimaging-biomarkers using mouse models with amyloid-precursor protein-transgene expression. *Prog Neurobiol.* 2011;95:547-556.

7. Zimmer ER, Leuzy A, Bhat V, Gauthier S, Rosa-Neto P. In vivo tracking of tau pathology using positron emission tomography (PET) molecular imaging in small animals. *Transl Neurodegener.* 2014;3:6.

8. Zimmer ER, Parent MJ, Cuello AC, Gauthier S, Rosa-Neto P. MicroPET imaging and transgenic models: a blueprint for Alzheimer's disease clinical research. *Trends Neurosci.* 2014;37:629-641.

9. Brendel M, Jaworska A, Griessinger E, et al. Cross-sectional comparison of small animal [18F]-florbetaben amyloid-PET between transgenic AD mouse models. *PLoS One.* 2015;10:e0116678.

10. Rominger A, Brendel M, Burgold S, et al. Longitudinal assessment of cerebral beta-amyloid deposition in mice overexpressing Swedish mutant beta-amyloid precursor protein using 18F-florbetaben PET. *J Nucl Med.* 2013;54:1127-1134.

11. Snellman A, Lopez-Picon FR, Rokka J, et al. Longitudinal amyloid imaging in mouse brain with 11C-PIB: comparison of APP23, Tg2576, and APPswe-PS1dE9 mouse models of Alzheimer disease. *J Nucl Med.* 2013;54:1434-1441.

12. Maruyama M, Shimada H, Suhara T, et al. Imaging of tau pathology in a tauopathy mouse model and in Alzheimer patients compared to normal controls. *Neuron.* 2013;79:1094-1108.

13. Okamura N, Furumoto S, Harada R, et al. Novel 18F-labeled arylquinoline derivatives for noninvasive imaging of tau pathology in Alzheimer disease. *J Nucl Med.* 2013;54:1420-1427.

14. Villemagne VL, Okamura N. In vivo tau imaging: obstacles and progress. *Alzheimers Dement.* 2014;10:S254-264.

15. Tago T, Furumoto S, Okamura N, et al. Synthesis and preliminary evaluation of 2-arylhydroxyquinoline derivatives for tau imaging. *J Labelled Comp Radiopharm.* 2014;57:18-24.

16. Dorr A, Sled JG, Kabani N. Three-dimensional cerebral vasculature of the CBA mouse brain: a magnetic resonance imaging and micro computed tomography study. *Neuroimage.* 2007;35:1409-1423.

17. Logan J, Fowler JS, Volkow ND, Wang GJ, Ding YS, Alexoff DL. Distribution volume ratios without blood sampling from graphical analysis of PET data. *J Cereb Blood Flow Metab.* 1996;16:834-840.

18. Constantinescu CC, Mukherjee J. Performance evaluation of an Inveon PET preclinical scanner. *Phys Med Biol.* 2009;54:2885-2899.

19. Rominger A, Mille E, Boning G, et al. alpha2-adrenergic drugs modulate the binding of [18F]fallypride to dopamine D2/3 receptors in striatum of living mouse. *Synapse.* 2010;64:654-657.

20. Santacruz K, Lewis J, Spires T, et al. Tau suppression in a neurodegenerative mouse model improves memory function. *Science.* 2005;309:476-481.

21. Fodero-Tavoletti MT, Okamura N, Furumoto S, et al. 18F-THK523: a novel in vivo tau imaging ligand for Alzheimer's disease. *Brain.* 2011;134:1089-1100.

22. Shah M, Catafau AM. Molecular Imaging Insights into Neurodegeneration: Focus on Tau PET Radiotracers. *J Nucl Med.* 2014;55:871-874.

23. Fodero-Tavoletti MT, Furumoto S, Taylor L, et al. Assessing THK523 selectivity for tau deposits in Alzheimer's disease and non-Alzheimer's disease tauopathies. *Alzheimers Res Ther.* 2014;6:11.

24. Crespo-Biel N, Theunis C, Borghgraef P, et al. Phosphorylation of protein Tau by GSK3beta prolongs survival of bigenic Tau.P301LxGSK3beta mice by delaying brainstem tauopathy. *Neurobiol Dis.* 2014;67:119-132.

25. Lemoine L, Saint-Aubert L, Marutle A, et al. Visualization of regional tau deposits using (3)H-THK5117 in Alzheimer brain tissue. *Acta Neuropathol Commun.* 2015;3:40.

26. Allen B, Ingram E, Takao M, et al. Abundant tau filaments and nonapoptotic neurodegeneration in transgenic mice expressing human P301S tau protein. *J Neurosci.* 2002;22:9340-9351.

27. Braak H, Braak E. Neuropathological stageing of Alzheimer-related changes. *Acta Neuropathol.* 1991;82:239-259.

28. Brendel M, Jaworska A, Herms J, et al. Amyloid-PET predicts inhibition of de novo plaque formation upon chronic gamma-secretase modulator treatment. *Mol Psychiatry.* 2015;20:1179-1187.

Figure 1

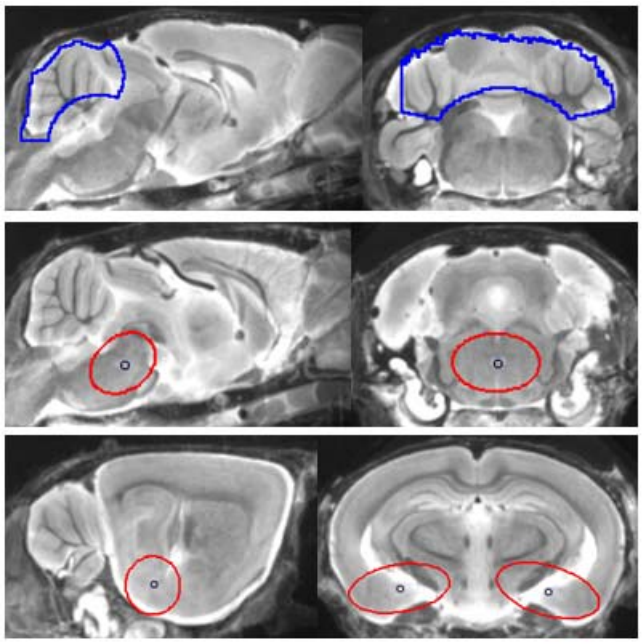

Definitions of VOIs projected on the mouse brain MRI atlas (*16*) in sagittal and coronal slices: Cerebellar VOI (top row; 55mm^3; blue line); oval-shaped brainstem VOI including central parts of the pons and the midbrain (middle row; 11mm^3; red line); bilateral spherical entorhinal cortex/amygdala (bottom row; 7mm^3 each; red line).

Figure 2

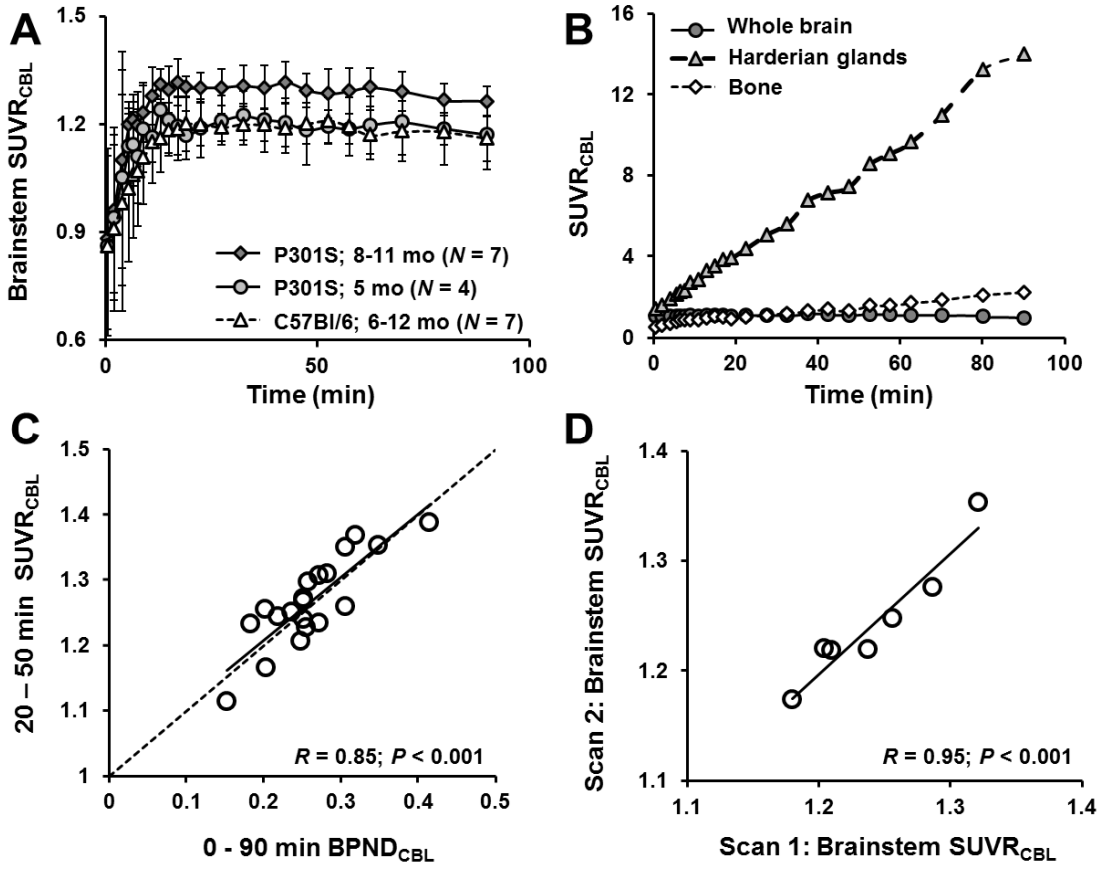

A) Brainstem/cerebellum ratios as functions of time following ^{18}F-THK5117 administration in groups of 5.5 and 8-11 month old transgenic P301S mice and pooled C57Bl/6 WT mice (6–12 months). Error bars are SD. B) Tissue/cerebellum ratios as functions of time following ^{18}F-THK5117 administration as assessed in the four mice with C57Bl/6 background demonstrating substantial cranial uptake. C) Correlation of ^{18}F-THK5117 BP_{ND} assessed from 90 minute dynamic μPET recordings with SUVR results (brainstem/cerebellum) from the 20-50 minute static frame, estimated from the brainstem VOI in all TG and WT mice. The dotted line is the line of identity (BP_{ND}=SUVR-1). D) Test-Retest correlation of brainstem/cerebellum SUVR in the static 20-50 minute frame.

Figure 3

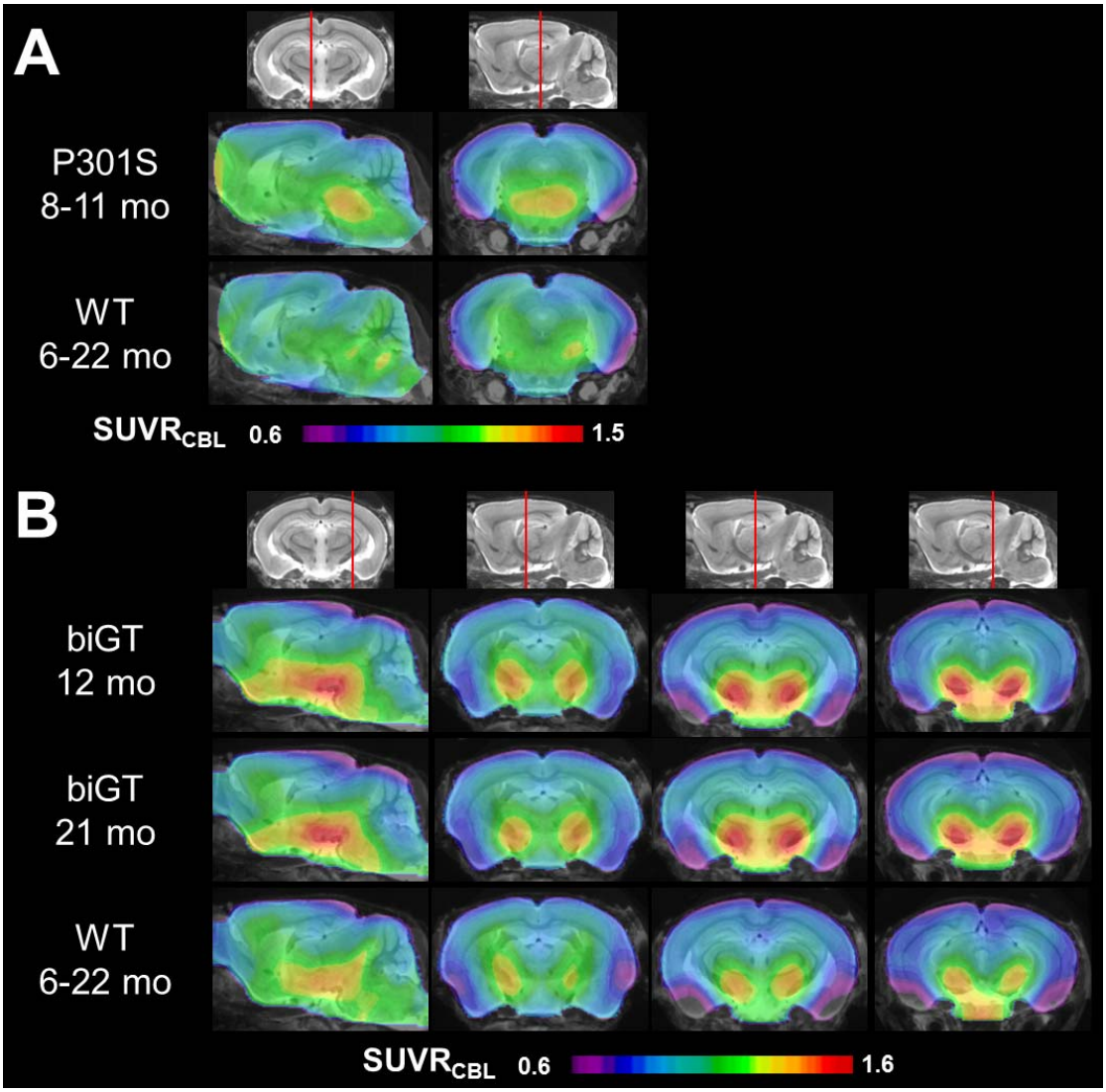

Mean parametric SUVR images in sagittal and coronal planes of ^{18}F-THK5117 uptake for aged P301S and WT controls (A), and likewise for young and old biGT and WT controls (B) projected upon an MRI mouse atlas (gray scale).

Figure 4

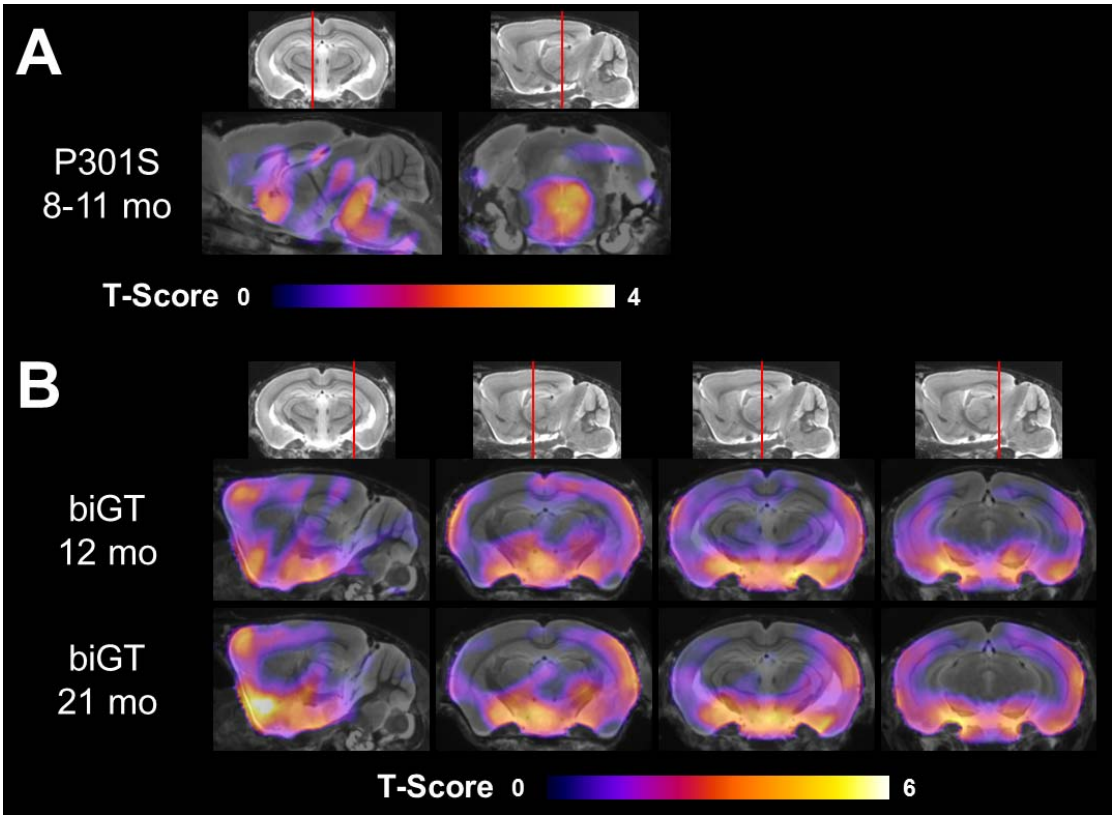

Mean voxel-wise Z-score maps in the sagittal and coronal planes of ^{18}F-THK5117 binding for groups of aged P301S vs pooled WT mice (A), and likewise for young and old biGT mice vs pooled WT mice (B). Results of the 2-sample *t*-test are expressed as Z-score maps projected upon an MRI mouse atlas (gray scale).

Figure 5

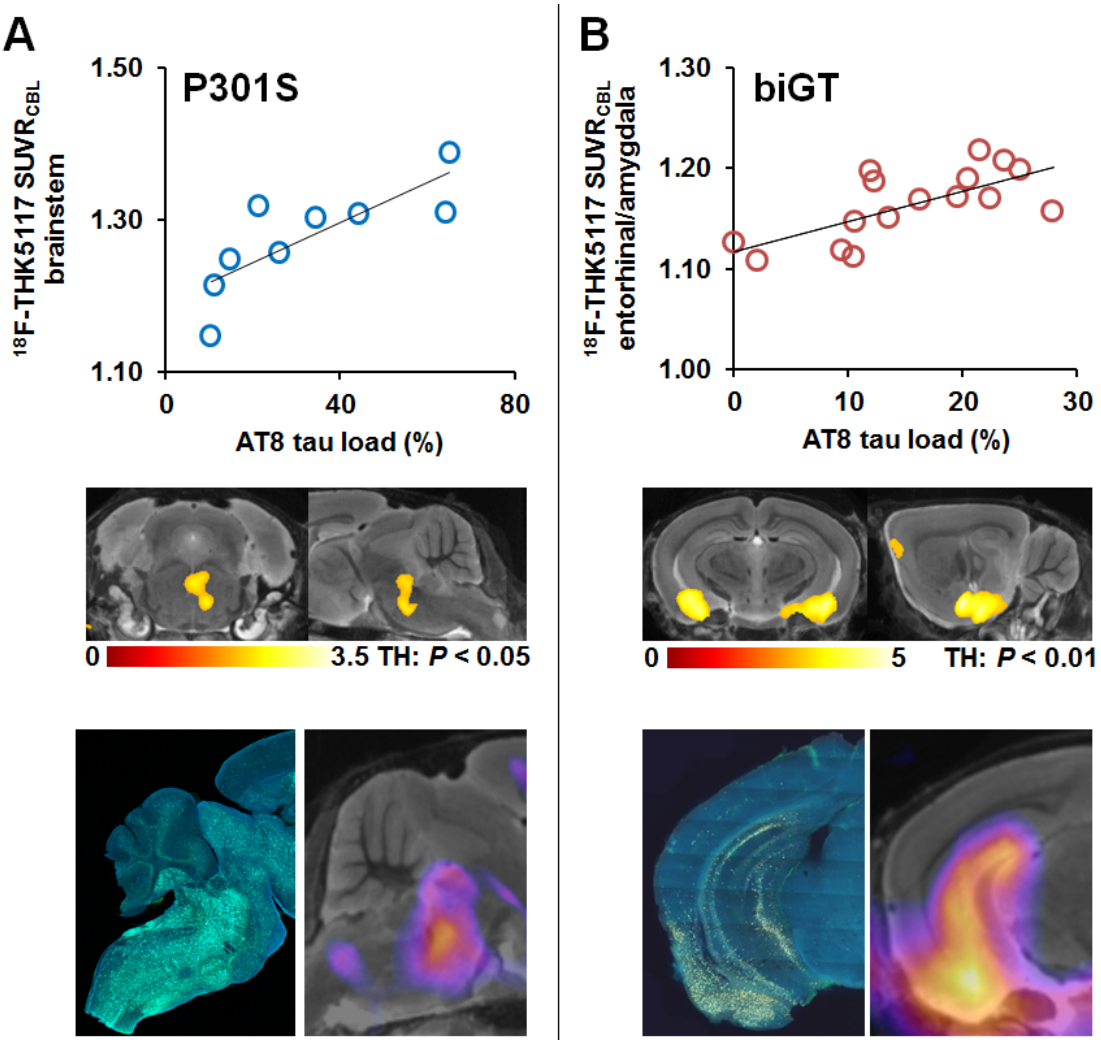

Validation of ^{18}F-THK5117 µPET results by immunohistochemical AT8 staining in vitro for P301S (A) and biGT (B) mice: Top row shows correlation plots of tau load (%) in corresponding AT8 stained areas with ^{18}F-THK5117 SUVR. Middle row depicts linear regression by SPM (uncorrected for multiple comparisons, k>20 voxels) between tau load (%) and µPET SUVR images projected upon an MRI mouse atlas. Bottom row illustrates AT8 stained sections from single mice along with their individual SPM derived Z-score maps (projected upon an MRI mouse atlas).

Figure 6

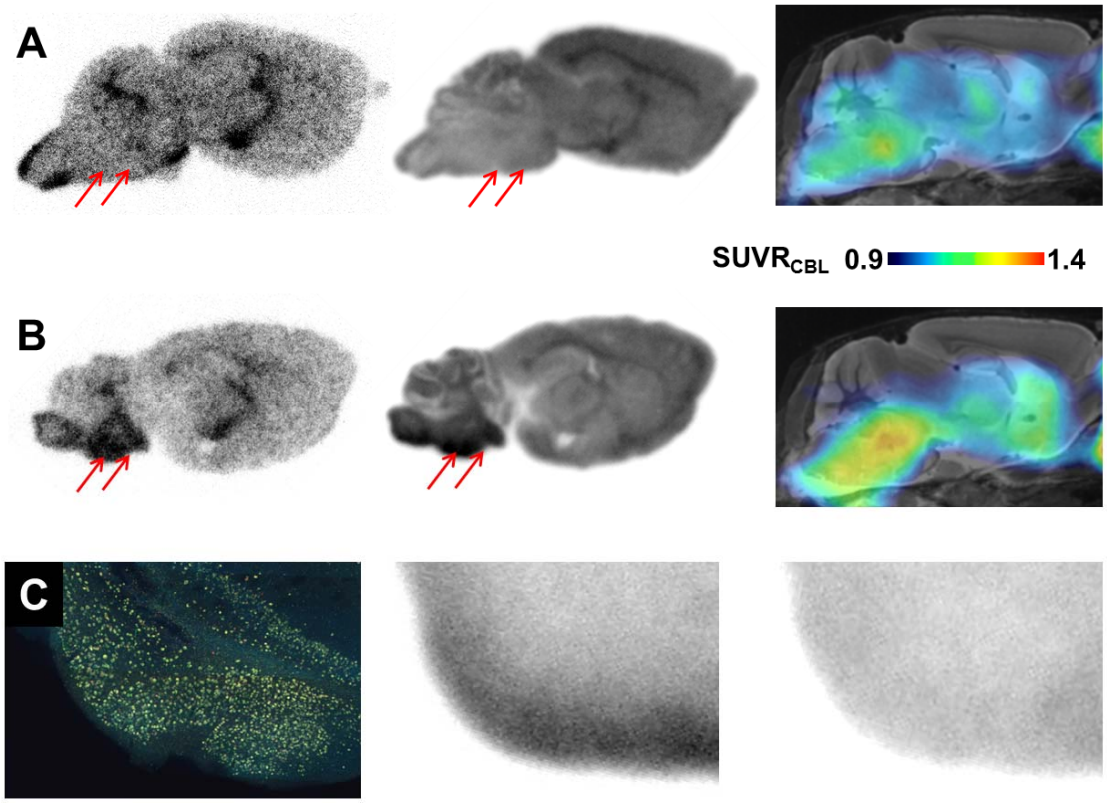

A) Corresponding sagittal planes for autoradiography *ex vivo* (50min p.i.), autoradiography *in vitro,* and µPET (SUVR$_{CBL}$ 20-50min p.i.) from an individual 12month old C57Bl/6 mouse expressing low ^{18}F-THK5117 uptake in the brainstem (red arrows). B) Corresponding sagittal planes for autoradiography *ex vivo* (50min p.i.), autoradiography *in vitro,* and µPET (SUVR$_{CBL}$; 20-50min p.i.) from an 11month old P301S mouse characterized by elevated ^{18}F-THK5117 uptake in the brainstem (red arrows). C) AT8 staining in the tau-rich entorhinal, post-piriform and amygdaloidal cortex of a biGT mouse aged 21months (coronal plane), along with corresponding *in vitro* autoradiography of ^{18}F-THK5117 binding without (middle panel) and with blocking (right panel) by excess non-radioactive THK5117.

Table 1 Study overview. *p<0.05; **p<0.01; ***p<0.001; 2-sample t-test.

Mouse Strain	Age (mo)	Weight (g; mean±SD)	µPET scan (N)	Immunohistochemistry AT8 Staining (N)	Autoradiography *ex vivo* (N)	Autoradiography *in vitro* (N)	µPET SUVR Brainstem (mean±SD)	AT8 Tau Load (%; mean±SD)
P301S	5.5	28.3±4.1	4	2	2	2	1.15±0.04	10.4/11.2
	8-11	26.1±5.8	7	7	3	3	1.31±0.05***	38.6±20.0
WT	6-22	30.4±4.8	25	2	5	5	1.17±0.05	0
							µPET SUVR Entorhinal/Amygdala (mean±SD)	
biGT	12	29.7±4.5	8	8		2	1.16±0.04***	11.4±7.4
	21	28.1±5.5	8	8		2	1.17±0.03***	14.3±5.8
WT	6-22	30.4±4.8	25	2	5	5	1.01±0.04	0